LETTER

Realization of Polytype Heterostructures via Delicate Structural Transitions from a Doped Mott Insulator

Realization of Polytype Heterostructures via Delicate Structural Transitions from a Doped Mott Insulator

Yanyan Geng(耿燕燕)[1,2†], Manyu Wang(王曼雨)[1,2†], Shumin Meng(孟淑敏)[1,2], Shuo Mi(米烁)[1,2], Chang Li(李畅)[1,2], Huiji Hu(胡会吉)[1,2], Jianfeng Guo(郭剑锋)[3], Rui Xu(许瑞)[1,2], Fei Pang(庞斐)[1,2], Wei Ji(季威)[1,2], Weichang Zhou(周伟昌)[4*], and Zhihai Cheng(程志海)[1,2*]

[1]*Key Laboratory of Quantum State Construction and Manipulation (Ministry of Education), School of Physics, Renmin University of China, Beijing 100872, China*
[2]*Beijing Key Laboratory of Optoelectronic Functional Materials & Micro-nano Devices, School of Physics, Renmin University of China, Beijing 100872, China*
[3]*Beijing National Laboratory for Condensed Matter Physics, Institute of Physics, Chinese Academy of Sciences, Beijing 100190, China*
[4]*Key Laboratory of Low-dimensional Quantum Structures and Quantum Control of Ministry of Education, School of Physics and Electronics, Hunan Research Center of the Basic Discipline for Quantum Effects and Quantum Technologies, Hunan Normal University, Changsha 410081, China*

(Received 3 December 2025; accepted manuscript online 8 January 2026)

Transition-metal dichalcogenides hosting multiple competing structural and electronic phases are thus ideal platforms for constructing polytype heterostructures with emergent quantum properties. However, controlling phase transitions to form diverse heterostructures inside a single crystal remains challenging. In this study, we realize vertical/lateral polytype heterostructures in a hole-doped Mott insulator via thermal annealing-induced structural transitions. Raman spectroscopy, atomic force microscopy and scanning Kelvin probe force microscopy confirm the coexistence of T-H polytype heterostructures. Atomic-scale scanning tunneling microscopy/spectroscopy measurements reveal the transparent effect in 1H/1T vertical heterostructures, where positive bias voltage induces in a pronounced superposition of the $\sqrt{13} \times \sqrt{13}$ CDW of the 1T-layer on the 1H-layer. By systematically comparing the 1T/1H and 1T/1T interfaces, we demonstrate that the metallic 1H-layer induces a Coulomb screening effect on the 1T-layer, suppressing the formation of CDW domain walls and forming more ordered electronic states. These results clarify the interfacial coupling between distinct quantum many-body phases and establish a controllable pathway for constructing two-dimensional polytype heterostructures with tunable electronic properties.

DOI: 10.1088/0256-307X/43/3/030705 CSTR: 32039.14.0256-307X.43.3.030705

Introduction. Layered transitionmetal dichalcogenides (TMDs) have emerged as ideal material platforms for exploring correlated electronic behaviors owing to their rich and tunable electronic states, including charge density waves (CDW),[1–3] quantum spin liquids,[4] superconductivity,[5–7] and Mott insulators.[8–10] Their intrinsic two-dimensional nature allows van der Waals polytype heterostructures to be constructed by combining monolayers with distinct structural phases while preserving the individual properties of each layer.[11–14] More importantly, interlayer interactions can strongly intertwine the characteristics of different components, giving rise to emergent electronic states that surpass the intrinsic behaviors of individual materials, such as topological nodal-point superconductivity,[15] interfacial Kondo physics,[16] charged interlayer excitons,[17] and interlayer charge transfer.[18,19] These phenomena highlight the substantial potential of polytyped heterostructures for engineering correlated quantum states. However, conventional methods for fabricating such heterostructures typically rely on artificial stacking or epitaxial growth,[20–23] suffer from inefficiency, susceptibility to impurities, and defects. Achieving controllable, high-quality, phase-pure polytype heterostructures within a single crystal remains challenging.

TaS_2, a prototypical TMDs material, serves as an exemplary material for exploring polytype heterostructures because of its rich crystal structure and phase-dependent electronic correlation properties.[24–27] Specifically, 1T-TaS_2 exhibits a Mott-insulating ground state,[28,29] whereas 1H-TaS_2 exhibits metallic and superconducting behavior at low temperatures.[30,31] Atomic-scale integration of these two electronically distinct phases offers an ideal platform for manipulating electron correlation and interlayer coupling. A series of emergent phenomena has been observed in such systems, including artificial heavy-fermion behavior,[32] chiral superconductivity,[33] two-component nematic superconductivity,[34] and Kondo-like responses.[35,36] Notably, external stimuli, such as lasers, temperature, or electric fields, can trigger a structural

†These authors contributed equally to this work.
*Corresponding authors. Email: wchangzhou@hunnu.edu.cn; zhihaicheng@ruc.edu.cn

phase transition from 1T-TaS_2 to 1H-TaS_2,[37–39] enabling the in situ construction of T-H polytype heterostructures within a single crystal. Furthermore, doping can drive the system into a critical regime of competing phases,[40,41] opening new avenues for heterostructure engineering and the manipulation of exotic electronic states. However, the direct realization of stable T-H polytype heterostructures starting from hole-doped Mott insulators has rarely been reported.

In this study, we successfully realized diverse polytype heterostructures in hole-doped 1T-TaS_2 crystals through thermally induced structural phase transitions. The formation of both vertical and lateral T-H heterostructures was confirmed using Raman spectroscopy, atomic force microscopy (AFM) and scanning Kelvin probe force microscopy (SKPM). High-resolution STM imaging further uncovers a distinct electronic transparency effect at 1H/1T interfaces under positive bias voltage, where the $\sqrt{13}\times\sqrt{13}$ CDW modulation of the underlying 1T-layer can be detected through the top metallic 1H-layer. Comparative investigations of the 1T/1H and 1T/1T heterostructures revealed that the 1T-layer was subjected to Coulomb screening by the metallic 1H-layer, which reduced intralayer electron correlations and suppressed the formation of phase domain walls. In this study, multidimensional polytype heterostructures were fabricated in a single crystal, providing a new platform for investigating the proximity effects between Mott insulating, metallic, and superconducting phases in two-dimensional materials.

Results and Discussion. 1T-TaS_2 is a prototypical platform for studying Mott physics because of its uniquely correlated electronic ground state. Its layered structure consists of Ta atoms sandwiched between two S layers, forming octahedral 1T coordinates as shown in Fig. 1(a). At low temperature, the ground CDW state of 1T-TaS_2 is characterized by the commensurate $\sqrt{13}\times\sqrt{13}$ superlattice of Star-of-David (SoD) clusters, as depicted in Figs. 1(b) and 1(c). Each SoD contains 13 Ta 5d electrons and 12 electrons of the outer Ta atom pair and forms six occupied CDW bands, leaving one unpaired electron of the central Ta atom in a half-filled flat band. This half-filled band further splits into the upper and lower Hubbard bands (UHB and LHB) owing to strong electron-electron correlations, resulting in a Mott insulator [Fig. 1(d)]. The Mott

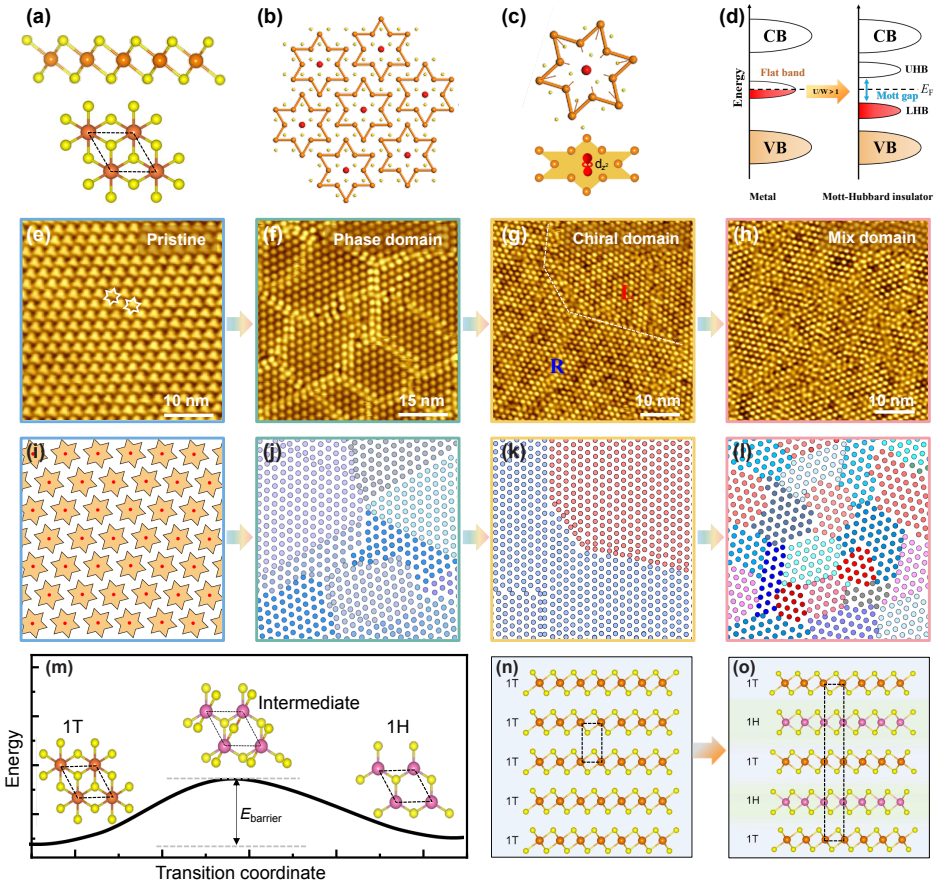

Fig. 1. Realization of polytype heterostructures via the doped Mott insulator. (a) Atomic structure model of monolayer 1T-TaS_2. (b) Schematic of the $\sqrt{13}\times\sqrt{13}$ SoD cluster superstructure. (c) Atomic models of the SoD cluster with the localized d_{z^2} orbital (unpaired electron) of central Ta atom. (d) Schematic band structures of correlated CDW state, where the half-filled flat band splits into UHB and LHB bands via electron correlations. (e)–(l) STM images and corresponding structure models of the pristine, low-hole-doped ($x=\sim0.77\%$), medium-hole-doped ($x=\sim2.5\%$), and high-hole-doped ($x=\sim5\%$) TaS_2. As the hole doping concentration increases, phase domains (f) and (g), chiral domains (g) and (k), and mixed domains (h) and (l) progressively appear. (m) Schematic energy landscape and top-view lattice structures of the 1T-phase (left), intermediate state (middle), and 1H-phase (right). $E_{barrier}$ denotes the energy barrier between the 1T- and 1H-phases. (n) and (o) Schematic illustration of the transition from the 1T phase (n) to the 4Hb-phase (o) in the doped Mott insulator. Scanning parameter: (e) $V=0.5\,V$, $I=100\,pA$; (f)–(h) $V=1.0\,V$, $I=120\,pA$.

insulating state is highly sensitive to carrier perturbations, making 1T-TaS_2 an ideal material for manipulating exotic quantum states.

Hole doping can effectively modify the flat-band filling factor and disturb the CCDW order of 1T-TaS_2, thereby triggering a sequence of novel quantum states.[27] Space scanning tunneling microscopy (STM) images and structural models reveal that hole doping disrupts the long-range CCDW order, gradually inducing the formation of phase domains, chiral domains, and mixed phase/chiral domains, as shown in Figs. 1(e)–1(l). Moreover, the introduction of holes weakens intralayer and interlayer interactions, pushing the system into a critical regime in which multiple electronic phases compete for similar energies. Consequently, hole-doped 1T-TaS_2 disrupts the original Mott insulating state as well as places the system in a tunable correlated phase space, laying the foundation for realizing polytype heterostructures.

Previous studies have shown that the energy difference between the 1T- and 1H-phases is extremely small [Fig. 1(m)]. The phase transition between 1T-phase and 1H-phase can be achieved by various external means such as laser excitation, STM-tip pulses, and thermal annealing.[37–39] Owing to the weakening of electron correlations induced by hole doping, the system can easily overcome the energy barrier between the 1T-phase and 1H-phase. Thermal annealing can further promote delicate structural transitions, enabling the transition from a doped Mott insulator to a polytype heterostructure, as illustrated in Figs. 1(n) and 1(o). These polytype heterostructures retain the electron correlations of the 1T-phase as well as introduce the metallic/superconducting state of the 1H-phase, providing a unique platform for studying the competition, coupling, and proximity effects between electron correlations, CDW, and superconductivity. Such a strategy of synergistic control through "doping and interface" to achieve structural transition significantly enriches the pathways for electronic state manipulation.

For low-hole-doped 1T-TaS_2, local lattice reconstruction and phase transitions can be induced when the annealing temperature rises above ~450 ℃. The optical microscopy images before and after annealing show

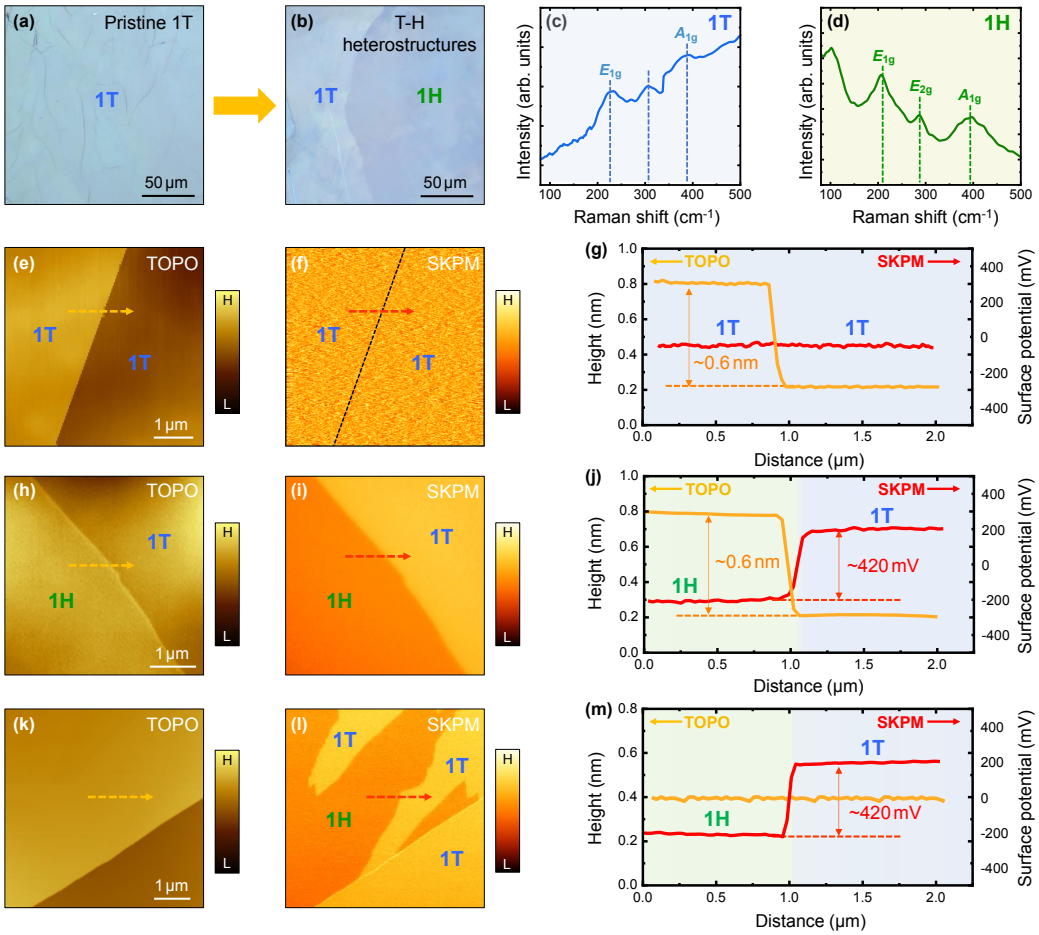

Fig. 2. Raman and SKPM characterization of the polytype heterostructures in low-hole-doped TaS_2. (a) and (b) Typical optical images of the TaS_2 before (a) and after (b) the formation of polytype heterostructures. (c) and (d) Raman spectra acquired from the 1T-phase (c) and 1H-phase (d) regions indicated in (a). Characteristic Raman modes of the 1T- and 1H-phases are marked with green and blue dashed lines, respectively. (e) and (f) AFM topography (e) and corresponding SKPM surface potential (f) images of a pristine 1T structure. (g) Line profiles extracted along the dashed lines in (e) and (f). The step height between adjacent 1T-layers is ~0.6 nm, with no significant surface potential difference observed. (h) and (i) AFM topography (h) and SKPM surface potential (i) images of vertical 1T-1H heterostructures. (j) Line profiles along the dashed lines in (h) and (i). The step height and surface potential difference between the 1T- and 1H-layers are ~0.6 nm and ~420 mV, respectively. (k) and (l) AFM topography (k) and SKPM surface potential (l) images of lateral 1T-1H heterostructures. (m) Line profiles along the dashed lines in (k) and (l). The surface potential difference between the 1T-domain and 1H-domain is ~420 mV.

significant color differences, which indicate the transition from 1T to T-H polytype heterostructures, as shown in Figs. 2(a) and 2(b). To further confirm this structural transition, Raman spectroscopy was performed on the different regions shown in Fig. 2(b). In the 1T-phase region [Fig. 2(c)], the Raman spectrum shows three characteristic peaks at approximately 240, 310, and 380 cm^{-1}, corresponding to the E_{1g} mode, the folded phonon mode related to the CDW, and the A_{1g} mode, respectively. In contrast, the Raman spectrum of 1H-phase exhibits the characteristic peaks at approximately 210, 285, and 400 cm^{-1} [Fig. 2(d)], corresponding to the E_{1g}, E_{2g}, and A_{1g} modes. The Raman spectra confirmed that thermal annealing drives structural reconstruction from the 1T-phase to the 1H-phase, achieving polytype heterostructures.

The AFM topography and SKPM surface potential images of the 1T-phase and polytype heterostructures are shown in Figs. 2(e)–2(m) and Fig. S1 in the Supplementary Materials (SM). For the pristine 1T-phase region [Figs. 2(e)–2(g)], the AFM topography shows a uniform layered structure with a step height of ∼0.6 nm. The corresponding SKPM image and line profile showed no observable surface potential difference between the different 1T-layers, reflecting their uniform Mott insulating properties. In the heterostructure, the 1T- and 1H-layers can be easily distinguished in the SKPM images by their relatively higher and lower surface potentials, respectively. The vertical heterostructures refer to interfaces formed by stacking different structural phases along the crystal c-axis direction, whereas lateral heterostructures refer to interfaces where different structural phases are adjacent within the same layer plane. To ensure consistency and clarity in the presentation, in this paper, 1H/1T denotes vertical heterostructures, and 1H-1T denotes lateral heterostructures.

In the vertical 1T/H heterostructure region [Figs. 2(h)–2(j)], the surface potential difference between 1T-layer and 1H-layer is ∼420 mV. Notably, this potential difference was higher than the values measured for intrinsic 4Hb-TaS_2 and Se-doped 4Hb-TaS_2.[42] We propose that hole doping decreases the work function of the 1T-phase, thereby increasing the potential difference relative to the 1H-phase. In contrast, isoelectronic Se doping primarily increases the interlayer spacing and weakens the interlayer coupling. This reduced coupling suppressed charge transfer, which increased the work function of the 1T-phase. Moreover, the SKPM results further demonstrated that a potential difference of ∼420 mV was present at the in-plane domain boundaries, confirming lateral T-H heterojunctions. Under the current Kelvin probe force microscopy measurement conditions and experimental accuracy, no discernible difference was observed in the surface potentials of the 1T-layer of the 1T/1H and 1T/1T heterostructures. The realization of such multidimensional polytype heterostructures provides a new pathway for directly studying both the vertical and lateral proximity effects between Mott insulators and metals/superconductors.

Figure 3 presents the atomic-scale STM characterizations of the vertical 1H/1T and 1H/1H polytype heterostructures, revealing distinct interfacial electronic

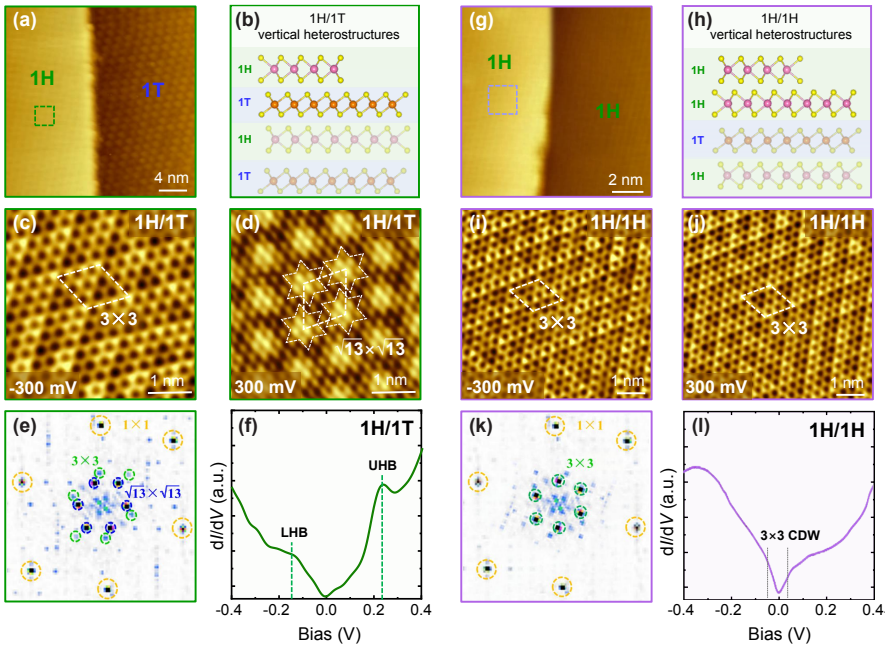

Fig. 3. Structure and electronic properties of vertical 1H/1T and 1H/1H heterostructures. (a) and (b) STM image and structure model of the 1H/1T heterostructure. (c) and (d) STM images acquired from the same region of the 1H/1T surface under negative (c) and positive (d) bias. At negative bias, the 3×3 CDW of the top 1H-layer is visible, whereas positive bias reveals the $\sqrt{13} \times \sqrt{13}$ CDW of the underlying 1T-layer. (e) The Fast Fourier transform (FFT) image of (d). The green and blue circles correspond to the 3×3 CDW and $\sqrt{13} \times \sqrt{13}$ CDW wavevectors, respectively. (f) $\mathrm{d}I/\mathrm{d}V$ spectra recorded from the 1H/1T surface. In addition to the quasi-3×3 CDW pseudogap of 1H-layer at the Fermi level, the UHB and LHB features of the 1T-layer are observed. (g) and (h) STM image and structure model of the vertical 1H/1H heterostructure. (i) and (j) STM images taken on the same region of 1H/1H surface under negative (i) and positive (j) bias. Only the 3×3 CDW pattern of the 1H/1H surface is visible. (k) FFT image of (j). (l) $\mathrm{d}I/\mathrm{d}V$ spectra of the 1H/1H surface, showing only the quasi-3×3 CDW pseudogap. Scanning parameter: (a), (c), (g), and (i) $V = -0.3$ V, $I = -200$ pA; (d) and (j) $V = 0.3$ V, $I = 200$ pA.

modulations arising from the different stacking configurations. Figures 3(a)–3(f) show the structural and electronic properties of vertical 1H/1T heterostructures. Under a negative bias (occupied state), the 1H/1T surface exhibited an intrinsic 3×3 CDW superlattice of the top 1H-layer, as marked by the green rhombus in Fig. 3(c). In contrast, under positive bias (unoccupied state), a pronounced electron transparency effect is observed, wherein the $\sqrt{13} \times \sqrt{13}$ periodic modulation of the underlying 1T-layer is superimposed upon the 3×3 pattern of 1H-layer [Fig. 3(d)]. The Fast Fourier transform (FFT) analysis further confirms the coexistence of these two periodicities, where the green and blue dashed circles correspond to the 3×3 and $\sqrt{13} \times \sqrt{13}$ wavevectors, respectively [Fig. 3(e) and Fig. S2 in the SM].

This bias-dependent behavior indicates that under a positive bias, electrons from the STM tip can tunnel through the top 1H-layer into the unoccupied states of the underlying 1T-layer. In contrast, under negative bias, the occupied states of the 1H-layer form an energy barrier, causing the tunneling current to mainly reflect the electronic states of the 1H-layer [Fig. S3 in the SM]. However, this simple tunneling-decay model cannot fully explain why the CDW modulation of the 1T-layer remains clearly visible despite the finite thickness of the 1H-layer and the presence of a van der Waals gap. To further understand the underlying mechanism, $\mathrm{d}I/\mathrm{d}V$ spectroscopy was performed in the 1H/1T region [Fig. 3(f)]. In addition to the quasi-3×3 CDW pseudogap near the Fermi level from the 1H-layer, the spectra clearly revealed the characteristic LHB and UHB features of the 1T-phase [Fig. S4 in the SM]. These results demonstrate that interlayer electronic coupling enables the correlated electronic states of the 1T-layer to effectively influence the local density of states in the 1H-layer, thereby further enhancing the visibility of the CDW modulation of the 1T-layer in the STM images. This observation is consistent with the interlayer interaction characteristics previously reported in 1H/1T TaS_2 heterostructures and 4Hb-TaS_2.[43,44]

We further conducted comparative studies on the vertical 1H/1H heterostructures, as depicted in Figs. 3(g)–3(l). The STM images acquired under both negative and positive biases [Figs. 3(i) and 3(j)] display only the intrinsic 3×3 CDW pattern of the 1H-phase. The $\mathrm{d}I/\mathrm{d}V$ spectrum of the 1H/1H region shows only a quasi-3×3 CDW pseudogap without any other electronic features, as shown in Fig. 3(l). This comparison confirms that the additional $\sqrt{13} \times \sqrt{13}$ modulation arises from interfacial electronic coupling unique to the polytype 1H/1T interface, providing evidence for interface-driven electronic modulation in correlated layered systems.

Figure 4 presents the structural properties of the vertical 1T/1T and 1T/1H polytype heterostructures, revealing the regulatory mechanisms of different stacking configurations on the CDW domain structure and internal interactions of the 1T-phase. As illustrated in Figs. 4(a) and 4(b), the 1T/1T surface exhibited a typical phase domain network, which is consistent with the bulk low-hole-doped 1T-TaS_2 sample. In contrast, the STM image of the 1T/1H surface displays a uniform and long-range

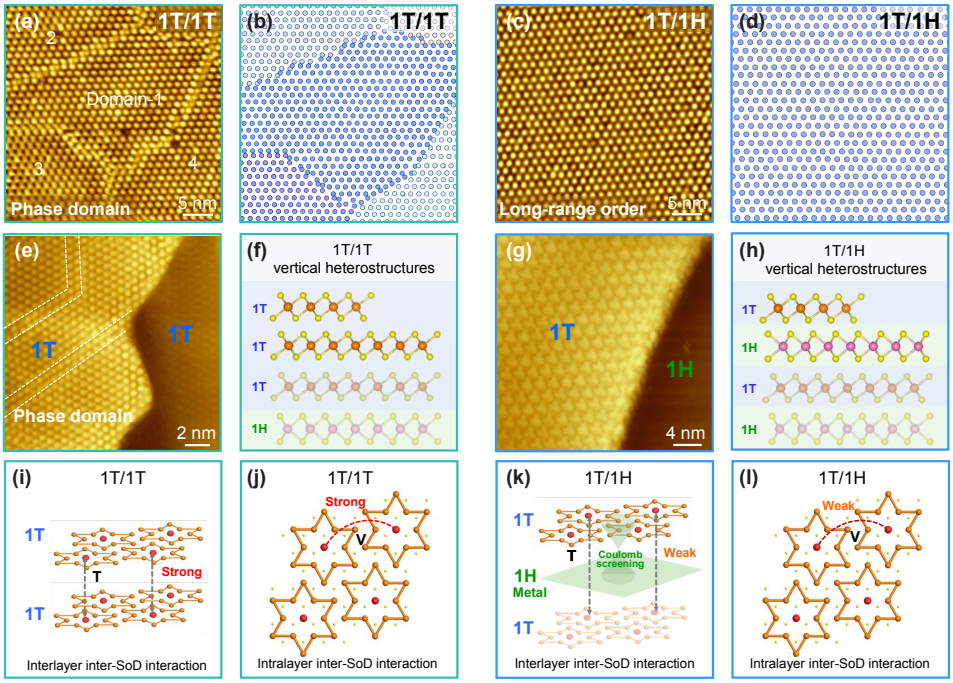

Fig. 4. Structure properties of vertical 1T/1H heterostructures. (a) and (b) STM image and schematic diagram of the 1T/1T surface, with the phase domain walls clearly visible. (c) and (d) STM image and schematic of the 1T/1H surface, where the phase domain walls are suppressed. (e) and (f) STM image and schematic diagram of the 1T/1T step edge. Phase domain walls in the top 1T-layer are indicated by white dashed lines. (g) and (h) STM image and schematic diagram of the 1T/1H step edge. (i) and (j) Schematics of interlayer (T) and intralayer (V) inter-SoD interactions in the 1T/1T configuration. The 1T/1T configuration is under strong interlayer and intralayer inter-SoD interactions. (k) and (l) Schematic of the interlayer (T) and intralayer (V) inter-SoD interactions of the 1T/1H configuration. The Coulomb screening effect from the metallic 1H-layer weakens the intralayer inter-SoD interactions, resulting in weak interlayer and intralayer inter-SoD interactions in 1T/1H configuration. Scanning parameter: (a) and (c) $V = 1.0\,\mathrm{V}$, $I = 100\,\mathrm{pA}$; (e) and (g) $V = 0.5\,\mathrm{V}$, $I = 100\,\mathrm{pA}$.

ordered structure with strongly suppressed domain walls [Figs. 4(c), 4(d), and Fig. S5 in the SM]. This indicates that the underlying metal 1H-layer exerts a significant modulating effect on the CDW domains of the 1T-layer. To further validate the influence of the different stacking configurations on the electronic order of the 1T-layer, the step edges of the 1T/1T and 1T/1H configurations are shown in Figs. 4(e)–4(h) and Fig. S6 in the SM. In the 1T/1T step region [Figs. 4(e) and 4(f)], the upper 1T-layer still exhibits a dense network of phase domain walls, marked by white dashed lines. In contrast, the domain structure was similarly weakened in the 1T/1H step region [Figs. 4(g) and 4(h)], which is consistent with the observations in Fig. 4(c). This agreement further confirms that the metallic 1H-layer effectively modulates the local electronic structure of the adjacent 1T-layer.

Figures 4(i)–4(l) illustrate the microscopic mechanism underlying the distinct behaviors of these heterostructures. In the 1T/1T configuration [Figs. 4(i) and 4(j)], both the interlayer inter-SoD interaction (T) and intralayer inter-SoD interaction (V) remain relatively strong.[27] As a result, the system stabilizes a strong correlated Mott-CDW state, thereby giving rise to abundant phase domains. Conversely, in the 1T/1H heterostructure [Figs. 4(k) and 4(l)], the 1H-layer weakens the interlayer coupling and reduces the interlayer inter-SoD interaction. Moreover, the free charge carriers within the metallic 1H-layer exert the coulomb screening effect on 1T-layer. This Coulomb screening effect weakens the intralayer inter-SoD interaction within the 1T-layer, ultimately resulting in the disappearance of CDW domain structures and the emergence of a long-range ordered electron distribution. These findings demonstrate that polytype stacking configurations offer an effective degree of freedom for tuning the correlation strength and CDW domain configuration in 1T-TaS_2. By designing 1H/1T and 1T/1T stacking sequences within a single crystal, synergistic control over electronic correlation, interlayer coupling, and phase domain structures can be achieved in single-crystal systems.

The interfacial electronic properties of the lateral heterojunctions were systematically investigated, as shown in Fig. 5. Large-scale AFM topography and SKPM surface

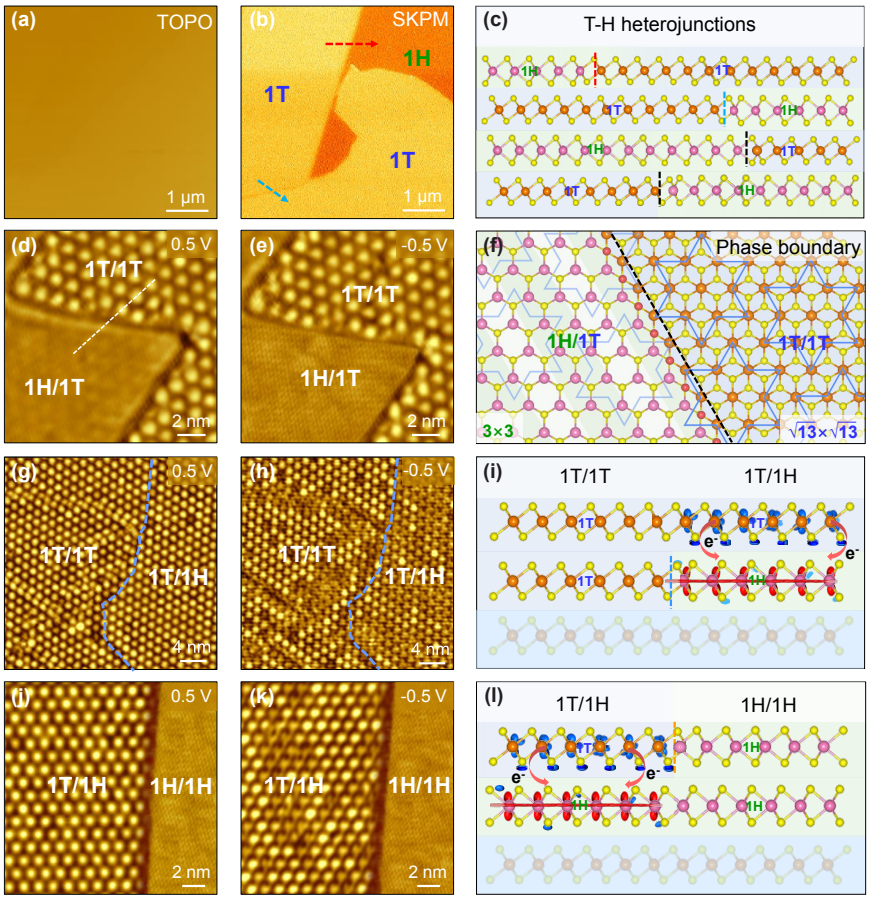

Fig. 5. Electronic properties of polytype lateral heterojunctions. (a) and (b) AFM topography (a) and SKPM surface potential (b) images of lateral 1T-1T and 1T-1H heterojunctions. (c) Lateral view of the polytype vertical/lateral T-H heterostructures. (d) and (e) STM images of lateral 1H/1T-1T/1T heterojunctions taken with positive (c) and negative (d) bias, with the SoD is distinctly observable under positive bias. The white dotted line indicates the directions of the SoD in the 1H/1T and 1T/1T. (f) Schematic of the lateral 1H/1T-1T/1T heterojunctions. The sharing S atoms at the phase boundary are highlighted by red, and the black dotted line indicates the phase boundary in the 1H/1T and 1T/1T. (g) and (h) STM images of lateral 1T/1T-1T/1H heterojunctions taken with positive (g) and negative (h) bias. (i) Schematic of the lateral 1T/1T-1T/1H heterojunctions. The charge transfers at the 1T/1H heterointerface contributes the apparent difference of 1T-layer at occupied and unoccupied states. Blue and red represent the electron depletion and accumulation regions. (j) and (k) STM images of lateral 1T/1H-1H/1H heterojunctions taken with positive (j) and negative (k) bias. (l) Schematic of the lateral 1T/1H-1H/1H heterojunctions.

potential images revealed micrometer-scale lateral 1T-1T and 1T-1H heterojunctions in TaS_2, as shown in Figs. 5(a)–5(c). Atomic-scale STM characterization further revealed rich electronic behavior at these lateral heterojunctions [Figs. 5(d)–5(l)]. At the lateral 1H/1T–1T/1T heterojunctions, the SoD superlattice can be resolved in the 1H/1T region under a positive bias, supporting the universality of the electronic transparency effect identified in vertical 1H/1T heterostructures. Notably, the orientations of the SoDs in the 1H/1T and 1T/1T regions are consistent, as indicated by the white dashed lines in Fig. 5(d). The structural model further showed that the top S atom arrangement remained nearly identical across the lateral phase boundary between the 1H- and 1T-phases, as shown in Fig. 5(f).

In contrast, the lateral 1T/1T–1T/1H heterojunctions displayed markedly different electronic properties. CDW domain walls were observed in the 1T/1T region, whereas the domain structure was strongly suppressed in the 1T/1H region [Fig. 5(g)], confirming the pronounced influence of the metallic 1H-layer on the CDW order of the 1T-layer. More intriguingly, under positive bias (unoccupied states), all SoD units in both 1T/1T and 1T/1H regions exhibit similar shapes and intensities. However, under a negative bias (occupied states), the number of bright SoDs in the 1T/1H region was significantly reduced compared to that in the 1T/1T region, displaying alternating bright and dark SoD patterns [Fig. 5(h), Figs. S6 and S7 in the SM]. This difference can be attributed to interlayer electron transfer at the 1T/1H heterointerface, as shown in Fig. 5(i). The STM images of the lateral 1T/1H–1H/1H heterojunctions further confirm that such charge transfer leads to distinct electronic structures in the occupied and unoccupied states of the 1T-layer [Figs. 5(j)–5(l)]. This behavior is consistent with the bright-dark SoD patterns induced by the partial charge transfer previously observed in Se-doped 4Hb-TaS_2,[42,45] which is distinct from the novel quantum states arising from CDW defects.[46]

Our findings reveal that doping-driven structural transitions can simultaneously construct both vertical and lateral polytype heterostructures within a single-crystal system. We identified universal electronic transparency and Coulomb screening effects at their interfaces. These discoveries provide pathways for modulating the correlated states, designing artificial polytype interfaces, and constructing functional heterostructures. In future, by further regulating the doping concentration, pulsed laser irradiation, or localized electric fields, it may be possible to achieve more complex and patterned polytype interfacial structures within the same material system.

Conclusion. In this study, both vertical and lateral polytype heterostructures were successfully realized within low-hole-doped 1T-TaS_2 via thermally induced structural transitions. Raman spectroscopy, SKPM, and STM/STS measurements collectively identify the coexistence of the 1T- and 1H-phases and resolve their distinct electronic characteristics at the atomic scale. At the 1H/1T interface, a pronounced electronic transparency effect emerges, where the CDW modulation of the underlying 1T layer becomes visible through the metallic 1H-layer. By comparing the 1T/1H and 1T/1T stacking configurations, we found that the metallic 1H-layer imposes a Coulomb screening effect on the neighboring 1T-layer, suppressing intralayer electronic correlations and eliminating the formation of CDW domains. Overall, our results establish a robust approach for creating high-quality polytype heterostructures within a single crystal, and provide a solid material basis for future low-dimensional quantum devices enabled by phase-engineered architectures.

Methods.

Sample Preparation. The high-quality 1T-$Ta_{1-x}Ti_xS_2$ single-crystals were grown by chemical vapor transport method. Ta (99.99%, Aladdin), $TaCl_5$ (99.99%, Aladdin), S (99.99%, Aladdin), and Ti (99.99%, Aladdin) powders with a nominal molar ratio of 1:0.02:2.05:x (x =∼0.77%, 2.5%, 5%) were mixed thoroughly and then loaded into quartz tubes. Large 1T-$Ta_{1-x}Ti_xS_2$ crystals with size up to 10 mm were collected for further characterization and measurement. X-ray diffraction and energy-dispersive X-ray spectroscopy were used to determine the crystal structure, morphology, and composition of the as-prepared samples. The Ti-doping contents of all the samples agreed with the nominal molar ratio of the source materials, demonstrating controllable synthesis. The polytype heterostructures were synthesized by heating low-hole-doped 1T-TaS_2 (x =∼0.77%) to 750 K in high vacuum ($<10^{-7}$ Torr) or in an argon purged glovebox.

STM. High-quality Ti-doped 1T-TaS_2 crystals were cleaved at room temperature in ultrahigh vacuum at a base pressure of 2×10^{-10} Torr, and directly transferred to the cryogen-free variable-temperature STM system (PanScan Freedom, RHK). Chemically etched W tips were used for STM measurements in constant-current mode. The STM tips were calibrated using a clean Ag(111) surface. Gwyddion was used for the STM data analysis.

Data Availability. The authors declare that the data supporting the findings of this study are available within the article and its Supplementary Materials.

Acknowledgments. This work was supported by the National Natural Science Foundation of China (Grant Nos. 92477128, 92580137, 92477205, 12374200, 11604063, 11974422, and 12104504), the National Key R&D Program of China (MOST) (Grant No. 2023YFA1406500), the Strategic Priority Research Program (Chinese Academy of Sciences, CAS) (Grant No. XDB30000000), and the Fundamental Research Funds for the Central Universities and Research Funds of Renmin University of China (Grant No. 21XNLG27). Y.Y. Geng was supported by the Outstanding Innovative Talents Cultivation Funded Programs 2023 of the Renmin University of China. This paper is an outcome of "Two-dimensional anisotropic series of materials $FePd_{2+x}Te_2$: a structural modulation study from the atomic scale to the mesoscopic scale" (RUC25QSDL128), funded by the "Qiushi Academic-Dongliang" Talent Cultivation Project at Renmin University of China in 2025.

References

[1] Carpinelli J M, Weitering H H, Plummer E W, and Stumpf R 1996 *Nature* **381** 398

[2] Wang W, Wang B, Gao Z, Tang G, Lei W, Zheng X, Li H, Ming X, and Autieri C 2020 *Phys. Rev. B* **102** 155115

[3] Lian C S, Si C, and Duan W H 2018 *Nano Lett.* **18** 2924
[4] Chen Y, Ruan W, Wu M, Tang S, Ryu H, Tsai H Z, Lee R L, Kahn S, Liou F, Jia C, Albertini O R, Xiong H, Jia T, Liu Z, Sobota J A, Liu A Y, Moore J E, Shen Z X, Louie S G, and Mo S K 2020 *Nat. Phys.* **16** 218
[5] Lu J M, Zheliuk O, Leermakers I, Yuan N F Q, Zeitler U, Law K T, and Ye J T 2015 *Science* **350** 1353
[6] Wan P, Peng Y, Shen J, Zhang X, Wang J, Luo X, Liu Z, Song T, Parkin S P, and Wang J 2023 *Nature* **619** 46
[7] Mak K F, Lee C, Hone J, Shan J, and Heinz T F 2010 *Phys. Rev. Lett.* **105** 136805
[8] Ma L, Ye C, Yu Y, Lu X F, Niu X, Kim S, Feng D, Tomanek D, Son Y W, Chen X H, and Zhang Y B 2016 *Nat. Commun.* **7** 10956
[9] Sipos B, Kusmartseva A F, Akrap A, Berger H, Forró L, and Tutiš E 2008 *Nat. Mater.* **7** 960
[10] Calandra M 2018 *Phys. Rev. Lett.* **121** 026401
[11] Novoselov K S, Mishchenko A, Carvalho A, and Castro Neto A H 2016 *Science* **353** aac9439
[12] Huang X, Wang T, Miao S, Wang C, Li Z, Lian Z, Taniguchi T, Watanabe K, Okamoto S, Xiao D, Shi S F, and Cui Y T 2021 *Nat. Phys.* **17** 715
[13] Mahatha S K, Phillips J, Corral-Sertal J, Subires D, Korshunov A, Kar A, Buck J, Diekmann F, Garbarino G, Ivanov Y P, Chuvilin A, Mondal D, Vobornik I, Bosak A, Rossnagel K, Pardo V, Fumega A O, and Blanco-Canosa S 2024 *ACS Nano* **18** 21052
[14] Lüpke F, Waters D, de la Barrera S C, Widom M, Mandrus D G, Yan J Q, Feenstra R M, and Hunt B M 2020 *Nat. Phys.* **16** 526
[15] Nayak A K, Steinbok A, Roet Y, Koo J, Margalit G, Feldman I, Almoalem A, Kanigel A, Fiete G A, Yan B, Oreg Y, Avraham N, and Beidenkopf H 2021 *Nat. Phys.* **17** 1413
[16] Fan K, Jin H, Huang B, Duan G, Yu R, Liu Z Y, Xia H N, Liu L S, Zhang Y, Xie T, Tang Q Y, Chen G, Zhang W H, Chen F C, Luo X, Lu W J, Sun Y P, and Fu Y S 2024 *Nat. Commun.* **15** 8797
[17] Castellanos-Gomez A, Duan X, Fei Z, Gutierrez H R, Huang Y, Huang X, Quereda J, Qian Q, Sutter E, and Sutter P 2022 *Nat. Rev. Methods Primers* **2** 58
[18] Hong X, Kim J, Shi S F, Zhang Y, Jin C, Sun Y, Tongay S, Wu J, Zhang Y, and Wang F 2014 *Nat. Nanotechnol.* **9** 682
[19] Policht V R, Mittenzwey H, Dogadov O, Katzer M, Villa A, Li Q, Kaiser B, Ross A M, Scotognella F, Zhu X, Knorr A, Selig M, Cerullo G, and Dal Conte S 2023 *Nat. Commun.* **14** 7273
[20] Geim A K and Grigorieva I V 2013 *Nature* **499** 419
[21] Chang L L and Esaki L 1979 *Prog. Cryst. Growth Charact.* **2** 3
[22] Zhou Z, Hou F, Huang X, Wang G, Fu Z, Liu W, Yuan G, Xi X, Xu J, Lin J, and Gao L 2023 *Nature* **621** 499
[23] Achari A, Bekaert J, Sreepal V, Orekhov A, Kumaravadivel P, Kim M, Gauquelin N, Pillai P B, Verbeeck J, Peeters F M, Geim A K, Milošević M V, and Nair R R 2022 *Nano Lett.* **22** 6268
[24] Fischer M H, Loder F, and Sigrist M 2011 *Phys. Rev. B* **84** 184533
[25] Dong H Y, Sun P H, Lei L, Geng Y Y, Guo J F, Li Y, Huang L, Xu R, Pang F, Ji W, Zhou W C, Liu Z, Lu Z Y, Gao H J, Liu K, and Cheng Z H 2023 arXiv:2301.05885 [cond-mat.mtrl-sci]
[26] Zhang H, Guo J, Mi S, Li S, and Cheng Z 2023 *Chin. J. Vac. Sci. Technol.* **43** 825 (in Chinese)
[27] Geng Y, Dong H, Wang R, Guo J, Mi S, Lei L, Li Y, Huang L, Pang F, Xu R, Yu W, Gao H J, Ji W, and Cheng Z 2025 *ACS Nano* **19** 7784
[28] Geng Y Y, Lei L, Dong H Y, Guo J F, Mi S, Li Y, Huang L, Pang F, Xu R, Zhou W C, Liu Z, Ji W, and Cheng Z H 2023 *Phys. Rev. B* **107** 195401
[29] Geng Y, Dong H, Wang R, Wang Z, Guo J, Mi S, Li Y, Pang F, Xu R, Huang L, Gao H J, Ji W, Wang S, Zhou W, and Cheng Z 2025 arXiv:2507.05756 [cond-mat.str-el]
[30] Gao J J, Si J G, Luo X, Yan J, Jiang Z Z, Wang W, Han Y Y, Tong P, Song W H, Zhu X B, Li Q J, Lu W J, and Sun Y P 2020 *Phys. Rev. B* **102** 075138
[31] Nayak A K, Steinbok A, Roet Y, Koo J, Margalit G, Feldman I, Almoalem A, Kanigel A, Yan B, Oreg Y, Avraham N, and Beidenkopf H 2021 *Nat. Phys.* **17** 1413
[32] Vaňo V, Amini M, Ganguli S C, Chen G, Lado J L, Kezilebieke S, and Liljeroth P 2021 *Nature* **599** 582
[33] Ribak A, Skiff R M, Mograbi M, Rout P K, Fischer M H, Ruhman J, Chashka K, Dagan Y, and Kanigel A 2020 *Sci. Adv.* **6** eaax9480
[34] Silber I, Mathimalar S, Mangel I, Nayak A K, Green O, Avraham N, Beidenkopf H, Feldman I, Klein A, Goldstein M, Banerjee A, Sela E, and Dagan Y 2024 *Nat. Commun.* **15** 824
[35] Bang J, Lee B, Yang H, Kim S, Wulferding D, and Cho D 2024 *Phys. Rev. B* **109** 195170
[36] Nayak A K, Steinbok A, Roet Y, Koo J, Feldman I, Almoalem A, Kanigel A, Yan B, Rosch A, Avraham N, and Beidenkopf H 2023 *Proc. Natl. Acad. Sci. U.S.A.* **120** e2304274120
[37] Yang L, Hu S, Hu G, Zhou W, Zhang Y, Dai T, Zhang Y, Zhang J, Liu C, Wang J O, Qiao J, Li Z, Shao Y, and Wu X 2025 *Adv. Mater. Interfaces* **12** 2500067
[38] Chen Y, Dai Y X, Zhang Y, Zhang C, Zhou L, Jia L, Wang W, Han X, Yang H, Liu L, Si C, Sun Q F, and Wang Y 2025 *ACS Nano* **19** 14808
[39] Wang Z, Sun Y Y, Abdelwahab I, Cao L, Yu W, Ju H, Zhu J, Fu W, Chu L, Xu H, and Loh K P 2018 *ACS Nano* **12** 12619
[40] Liu J, Yao D, and Wu W 2025 *Chin. Phys. Lett.* **42** 080711
[41] Li H, Wang Z, Fan S, Li H, Yang H, and Wen H 2024 *Chin. Phys. Lett.* **41** 057402
[42] Geng Y, Guo J, Meng F, Wang M, Mi S, Huang L, Xu R, Pang F, Liu K, Wang S, Gao H J, Zhou W, Ji W, Lei H, and Cheng Z 2024 *Phys. Rev. B* **110** 115107
[43] Wen C H, Gao J J, Xie Y, Zhang Q, Kong P F, Wang J H, Jiang Y L, Luo X, Li J, Lu W J, Sun Y P, and Yan S C 2021 *Phys. Rev. Lett.* **126** 256402
[44] Ayani C G, Bosnar M, Calleja F, Solé A P, Stetsovych O, Ibarburu I M, Rebanal C, Garnica M, Miranda R, Otrokov M M, Ondrácek M, Jelínek P, Arnau A, and Vázquez de Parga A L 2024 *Nano Lett.* **24** 10805
[45] Crippa L, Bae H, Wunderlich P, Mazi I I, Yan B H, Sangiovanni G, Wehling T, and Valentí R 2024 *Nat. Commun.* **15** 1357
[46] Yang W, Karbasizadeh S, Jeon H, Hus S, Baddorf A P, Mu S, Berlijn T, Zhou H D, Ko W, and Li A P 2025 *Phys. Rev. B* **112** 245126